Supporting information

Iron electrodes based on sulfur-modified iron oxides with enhanced stability for iron-air batteries

Nicolás Villanueva[1], Cinthia Alegre[1,], Javier Rubin[2,3], Horacio A. Figueredo-Rodríguez[4,†], Rachel D. McKerracher[4], Carlos Ponce de León[4], María Jesús Lázaro[1,*]*

[1]Instituto de Carboquímica, Consejo Superior de Investigaciones Científicas. C/. Miguel Luesma Castán, 4, 50018, Zaragoza (Spain)

[2] Instituto de Nanociencia y Materiales de Aragón (INMA), CSIC-Universidad de Zaragoza, 50009, Zaragoza (Spain)

[3] Departamento de Ciencia y Tecnología de Materiales y Fluidos, Universidad de Zaragoza, 50018 Zaragoza (Spain)

[4]Electrochemical Engineering Laboratory, Energy Technology Research Group, Faculty of Engineering and Physical Sciences, Southampton University, Southampton, SO17 1BJ (UK)

[†] Escuela de Ingeniería y Ciencias, Tecnológico de Monterrey, CCM, 14380, CDMX, (México)

***Corresponding authors:** cinthia@icb.csic.es; mlazaro@icb.csic.es

S.1. Experimental details

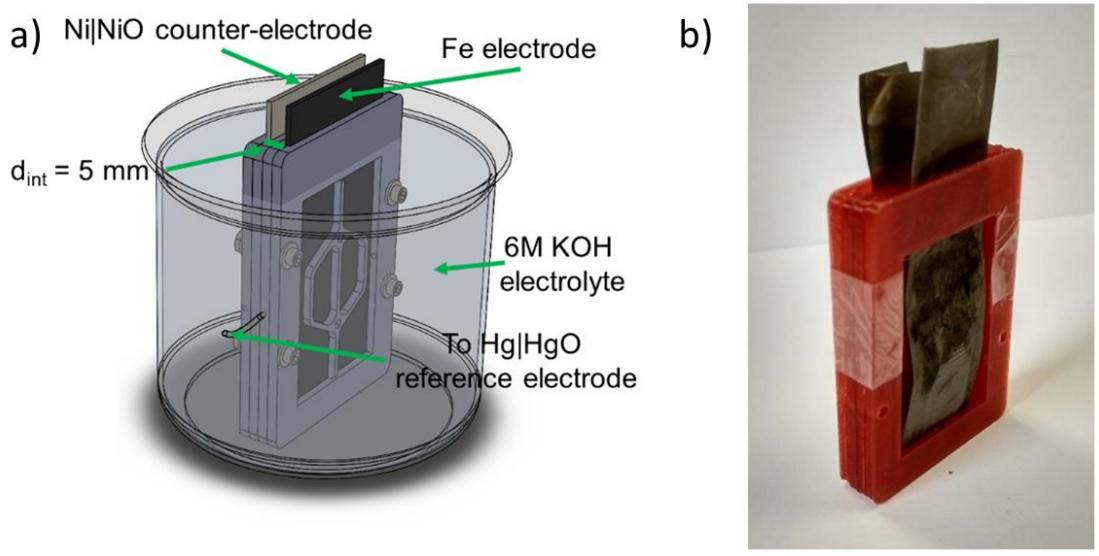

Figure S1. a) Schematic view of the holder employed for the electrochemical tests, b) Image of the holder containing the working electrode and counter electrode.

A scheme and an actual photograph of the electrodes system and cell is shown in **Figure S1**. The reference and counter electrodes are held only 5 mm apart to reduce the electrical resistance in the electrolyte and the overpotential related to it. The reference electrode is connected through a capillary, contacting close to the working electrode.

S.2. Additional physical-chemical characterization

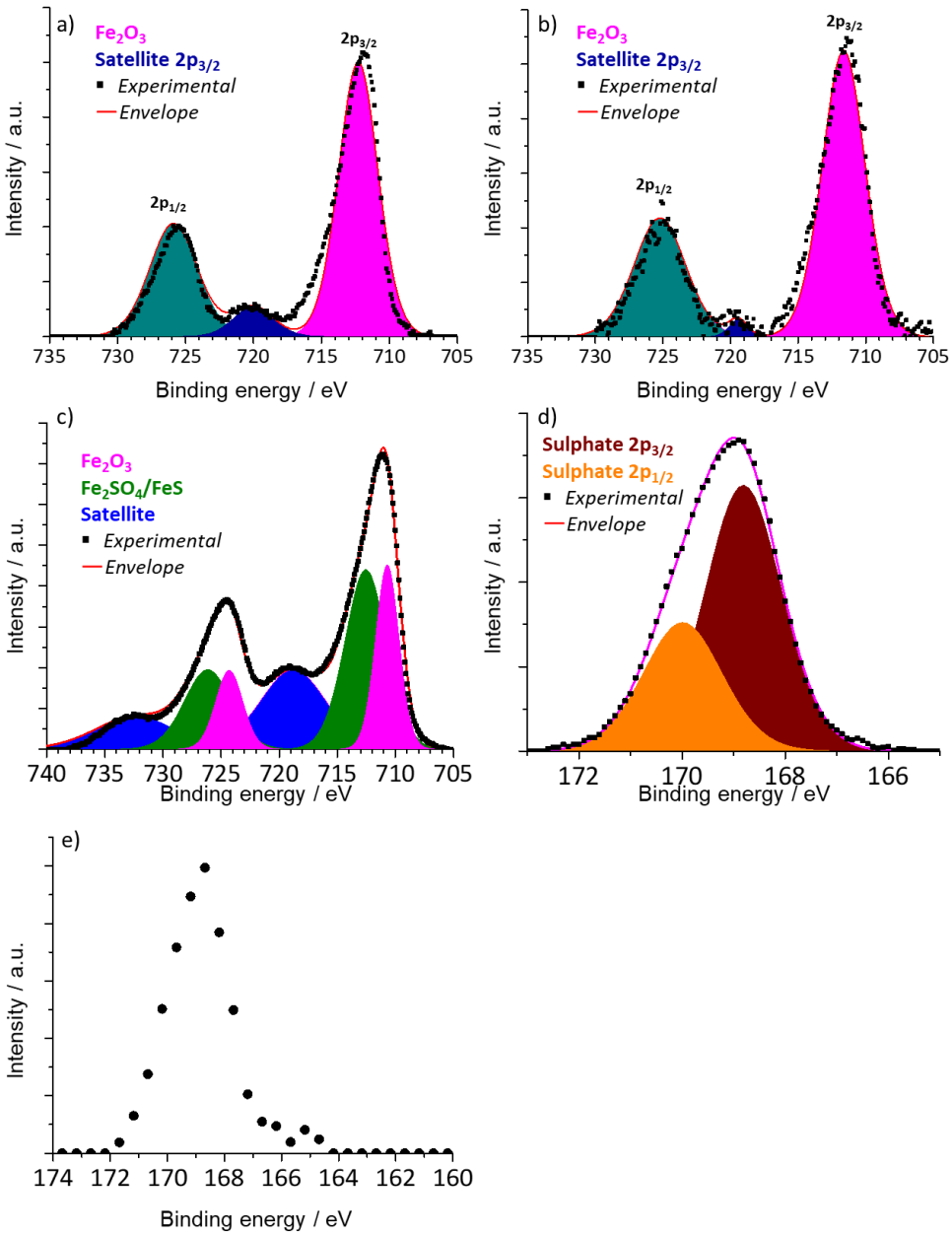

Figure S2. High-resolution XPS spectra of Fe2p in a) Fe_2O_3-COM and b) Fe_2O_3-OXL. High-resolution XPS spectra of (c) Fe2p and (d) S2p in S-Fe_2O_3-SHX. e) High-resolution XPS spectra of S2p in S-Fe_2O_3-OXL with a wider B.E. range.

Table S1. Mössbauer hyperfine parameters for samples Fe_2O_3-OXL, S-Fe_2O_3-OXL, Fe_2O_3-SHX and S-Fe_2O_3-SHX.

	Fe_2O_3-OXL		**S-Fe_2O_3-OXL**			**Fe_2O_3-SHX**		**S-Fe_2O_3-SHX**		
	S1	S2	S1	S2	D	S1	D	S	D1	D2
B_{hf} (T)	51.62(1)	49.54(2)	51.66(1)	49.60(2)	–	45.1[(b)]	–	43.3[(b)]	–	–
δ (mm/s)	0.374(1)	0.325(2)	0.372(1)	0.318(1)	0.382(5)	0.33[(b)]	0.29(2)	0.346[(b)]	0.377(5)	0.369(1)
2ε/QS (mm/s)[(a)]	–0.208(1)	0[(c)]	–0.208(1)	0[(c)]	0.760(8)		0.60(3)	–0.204(2)	1.144(3)	0.72(2)
FWHM (mm/s)	0.250(2)	0.474(7)	0.231(2)	0.504(5)	0.71(1)		0.83(8)		0.311(5)	0.50(1)
Area (%)	76.1(1)	23.9(1)	52.6(1)	40.7(1)	6.7(1)	96.9(3)	3.1(5)	71.2(1)	15.5(1)	13.3(1)

Isomer shifts δ relative to α-Fe.

(a) 2ε for sextets, QS for doublets.

(b) Weighted average values. Median values of B_{hf}: 49.1 T for Fe_2O_3-SHX, 46.9 T for S-Fe_2O_3-SHX.

(c) Fixed values.

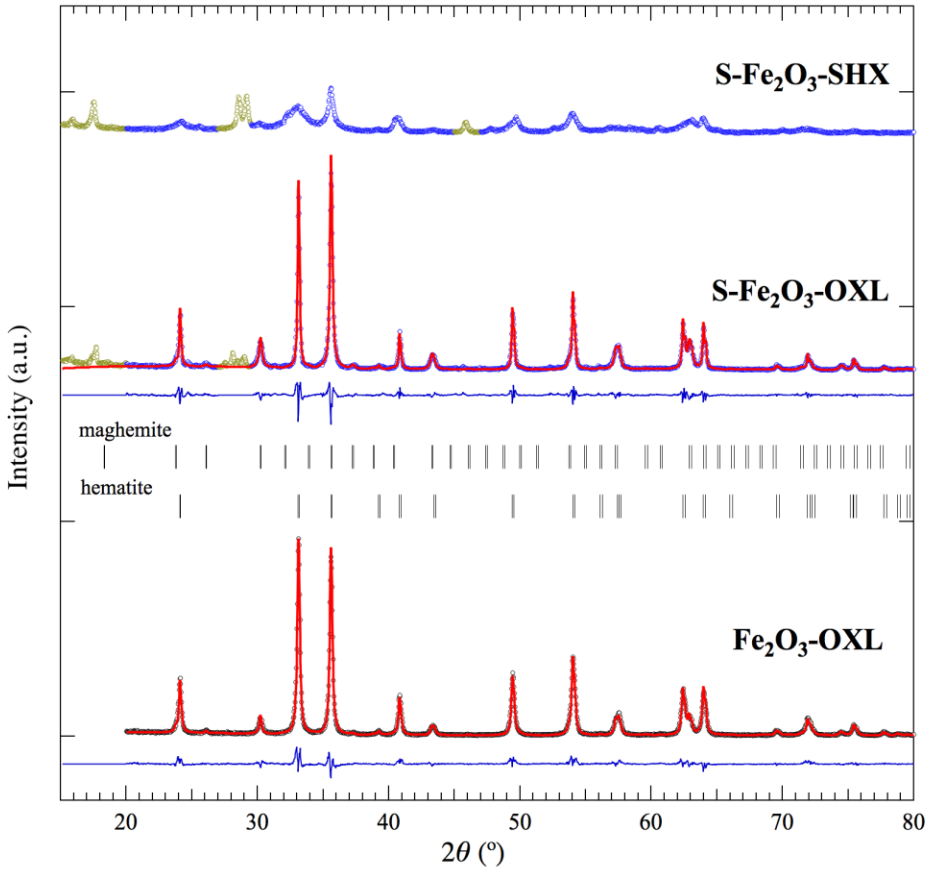

Figure S3. Experimental diffraction patterns (dots), fitted patterns (thick lines) and difference patterns (thin lines). Vertical lines show calculated reflection positions for maghemite (upper) and hematite (lower). Regions excluded from the fits carried out to determine the relative maghemite and hematite mass fractions are shown in green.

Figure S4a and **S4**b shows FTIR spectra for the different iron oxides, evidencing clear differences between samples. All the iron oxides, present absorption peaks observed at 3429 and 1630 cm^{-1} that are assigned to the stretching mode of hydroxyl group of water molecules. **Figures S4**c to **S4**f show the region from 1600 to 400 cm^{-1} for all the individual samples. Typical modes of maghemite are present in the FTIR spectra for the commercial sample, Fe_2O_3-COM (**Figure S4**c), composed of pure maghemite (γ-Fe_2O_3), as also determined by XRD. Klotz et al. mentioned well defined spectrum with peaks at 560, 587, 636, 690, 724 cm^{-1}, because of the vacancies in octahedral sides of γ-Fe_2O_3, also visible in our Fe_2O_3-COM sample, what corroborates its crystallographic structure [1]. On the other hand, S-Fe_2O_3-SHX shows two characteristic bands at 889 cm^{-1} and 796 cm^{-1} assigned to Fe-O-H bending vibrations as well as typical bands associated to hematite, in the range within 662-526 cm^{-1} and 494-437 cm^{-1} as referred by [2]. On the other hand, Fe_2O_3-OXL and S-Fe_2O_3-OXL show a mixed FTIR spectra with bands typical from both hematite (bands at 637, 538 and 462 cm^{-1}) and maghemite (bands at 694 and 480 cm^{-1}) (in accordance to XRD). Besides S-Fe_2O_3-OXL shows four bands at 1227, 1139, 1074 and 1000 cm^{-1} that could be assigned to adsorbed sulfates groups. Gotic et al. also described the presence of adsorbed sulphates on iron oxides obtained at acidic pH values, as is the case for S-Fe_2O_3-OXL [3,4].

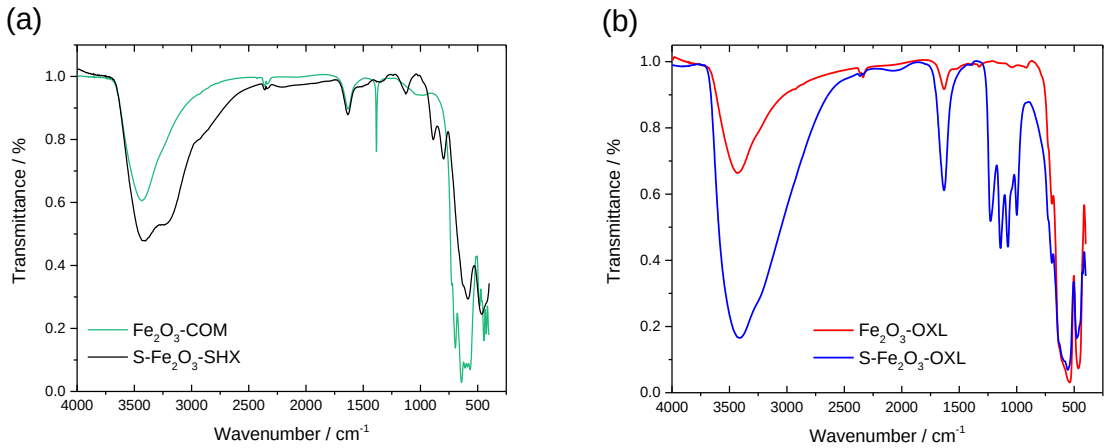

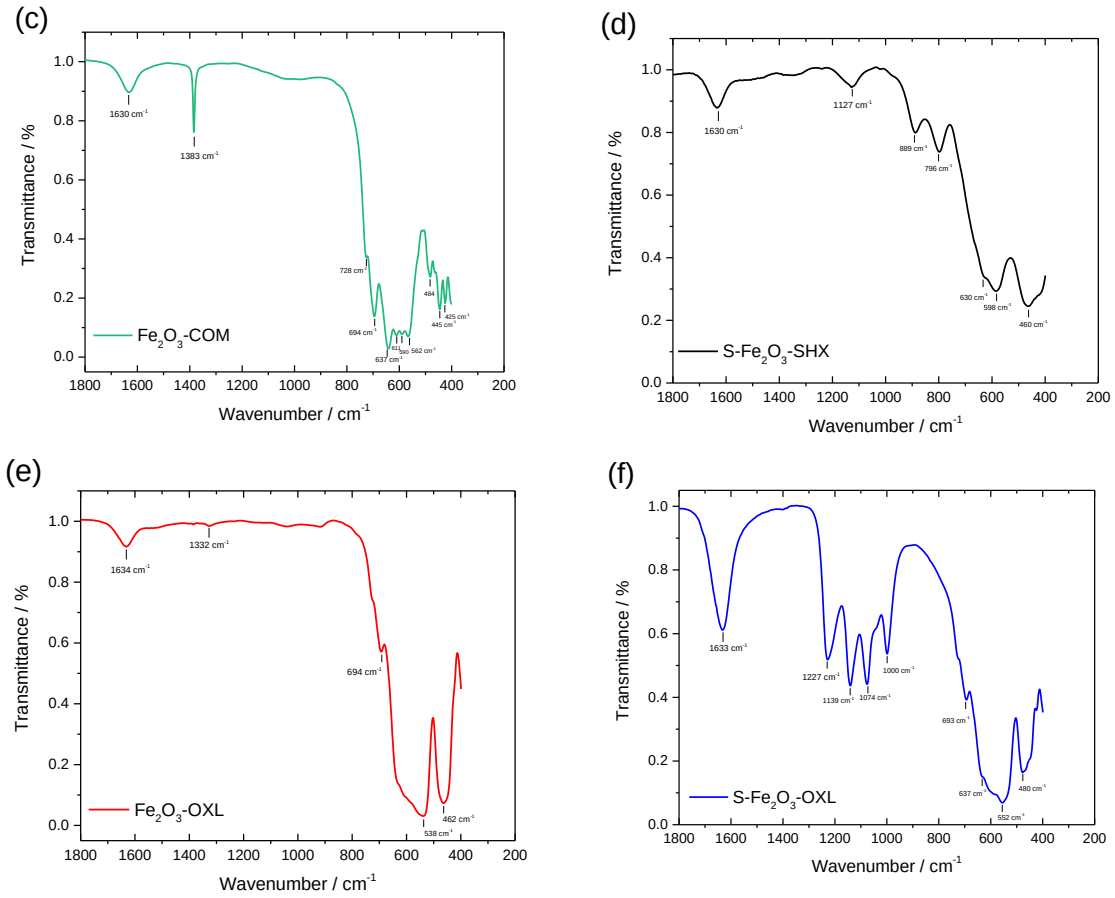

Figure S4. FTIR spectra for the different iron oxides synthesized: (a) Comparison between Fe_2O_3-COM vs. S-Fe_2O_3-SHX; (b) Comparison between Fe_2O_3-OXL vs. S-Fe_2O_3-OXL; (c) Fe_2O_3-COM (d) S-Fe_2O_3-SHX (e) Fe_2O_3-OXL (f) S-Fe_2O_3-OXL

Table S2 shows the quantitative results obtained from the fitting of N_2-adsorption/desorption isotherms (**Figure S5**a), along with the average porosity of the obtained samples, calculated from the ratio between the pore volume and the density (being the density considered for iron oxide: 5.26 g cm^{-3})[5]. Iron oxides obtained present a porosity around 50 %, which will be useful to hold the change of volume of the iron products during discharge. Commercial iron oxide presents the lowest pore volume and porosity of all the oxides. In Fe_2O_3-COM, the pores exist due to the small particle size, which creates small voids between the particles, as can be ascribed from the TEM image shown in **Figure 3**k (in the main manuscript). The regular shape of its particles allows the particles to stack better, and fewer voids are left in between, as can be seen in the mentioned image (**Figure 3**k).

In the case of Fe_2O_3-OXL and S-Fe_2O_3-OXL, the mesoporosity is consequence of the pores open in the bulk of the material by the decomposition of the organic salt. As a result, Fe_2O_3-OXL and S-Fe_2O_3-OXL have an almost identical surface area, around 55 m^2 g^{-1} which is the double of S-Fe_2O_3–SHX and around 33% larger than the surface area of the commercial sample, Fe_2O_3-COM (Table S2). Iron oxides obtained from oxalic acid present an average pore size around 14 nm, a similar value to the one of the commercial iron oxide. Whereas S-Fe_2O_3-SHX (obtained by precipitation with NaOH) presents the largest average pore size, ca. 24 nm. The use of NaOH in the synthesis might act as pore generator, favoring a larger pore size [6]. In any case, large mesopores may help accommodating the volume changes of the electrodes upon cycling. **Figure S5**b shows the pore size distribution of the iron oxides.

Table S2. Textural properties of the iron oxides

Sample	BET surface area / m^2 g^{-1}	Pore volume / cm^3 g^{-1}	BJH pore size / nm	Porosity
Fe_2O_3-COM	38.9	0.13	13.3	40 %
Fe_2O_3-OXL	55.5	0.24	14.6	55 %
S-Fe_2O_3-OXL	55.8	0.20	14.9	51 %
S-Fe_2O_3-SHX	28.3	0.19	23.8	50 %

Figure S5a shows the nitrogen physisorption isotherms for the four different iron oxides. The two oxides synthesized *via* precipitation with oxalic acid have a larger total pore volume (as can be ascribed from the maximum adsorbed quantity) and a larger surface area (seen from the slope at relative pressure 0.05 – 0.3) than the two other oxides. In addition, Fe_2O_3-OXL and S-Fe_2O_3-OXL (**Figure S5**b) have pores around 10 nm and 40-45 nm wide (Fe_2O_3-OXL has three times more 10 nm pore volume than S-Fe_2O_3-OXL), while S-Fe_2O_3-SHX and Fe_2O_3-COM only have 35 – 40 nm pores.

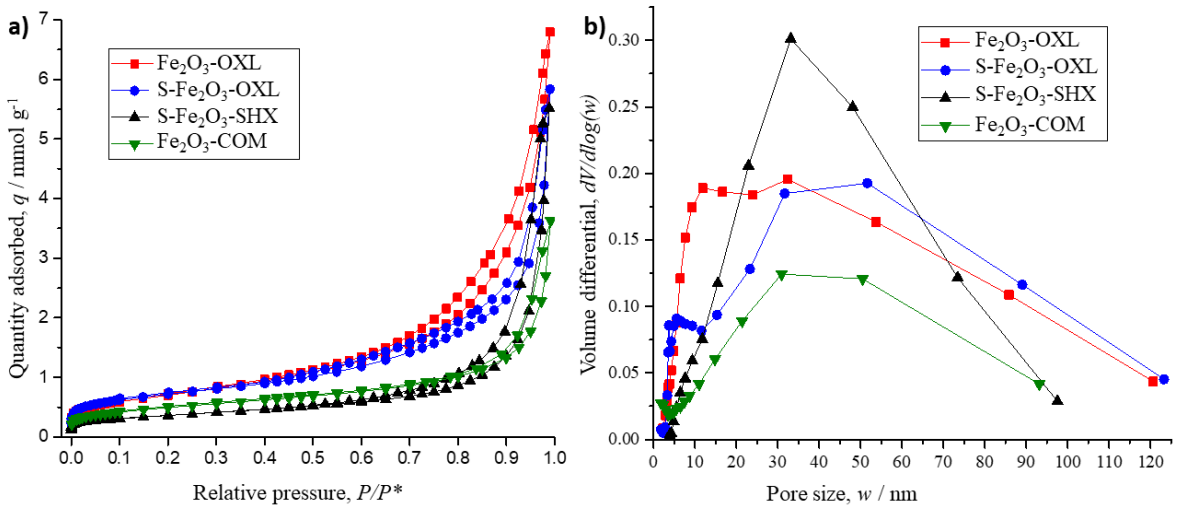

Figure S5. a) Nitrogen adsorption-desorption isotherms at 77K over the four synthesized iron oxides. b) Pore size distribution of the iron oxides

STEM-EDS analyses confirmed that sulfur is present along all of the iron particles (Figure S6).

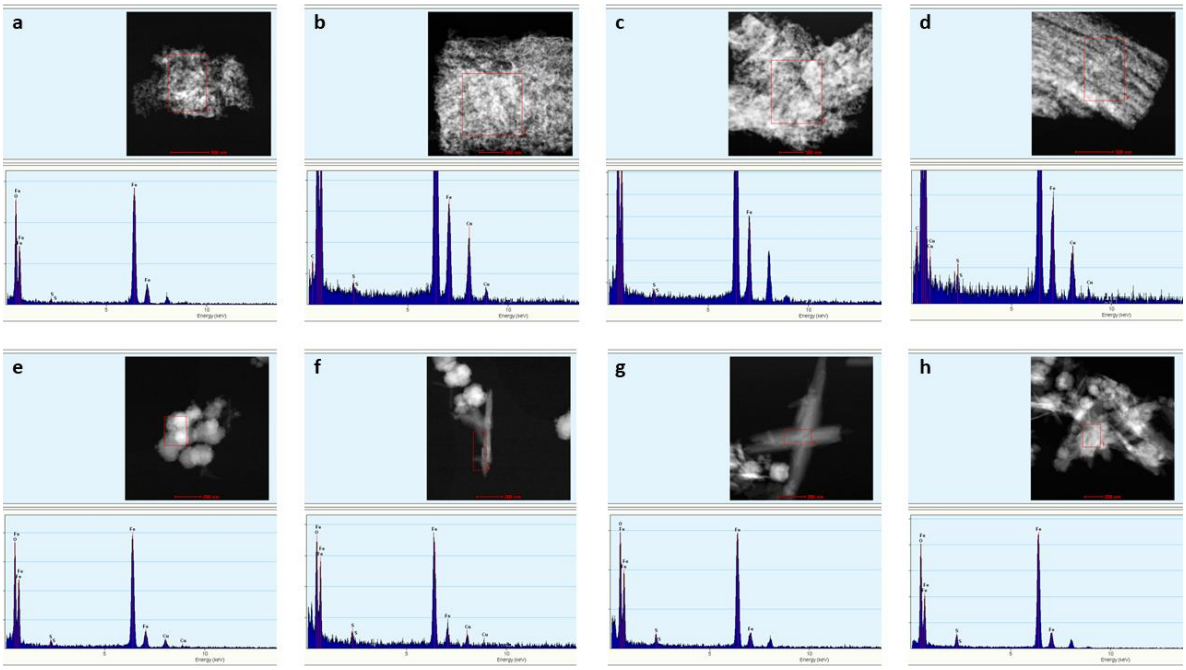

Figure S6. STEM images and EDS analysis of different iron crystallites in composites S-Fe_2O_3-OXL/C (a, b, c, and d) and S-Fe_2O_3-SHX/C (e, f, g and h)

Post-mortem XRD of the S-Fe_2O_3-OXL/C electrode after the first charge step, first discharge step and second discharge step are shown in **Figure S7**. It was not possible to see any sulfur phases. Only the sample examined after the second discharge step shows clear presence of goethite, but it was not possible to quantify the phases, as most of the peaks of Fe_3O_4 and $Fe(OH)_2$ overlap or are very close.

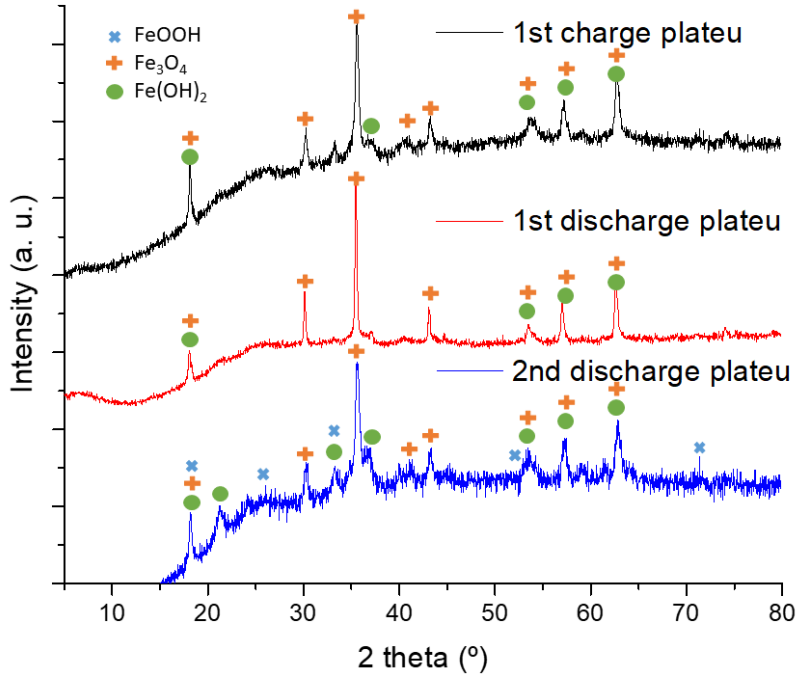

Figure S7. X-ray diffraction spectra of S-Fe_2O_3-OXL/C electrodes after the first charge plateau (top), first discharge plateau (middle) and second discharge plateau (bottom)

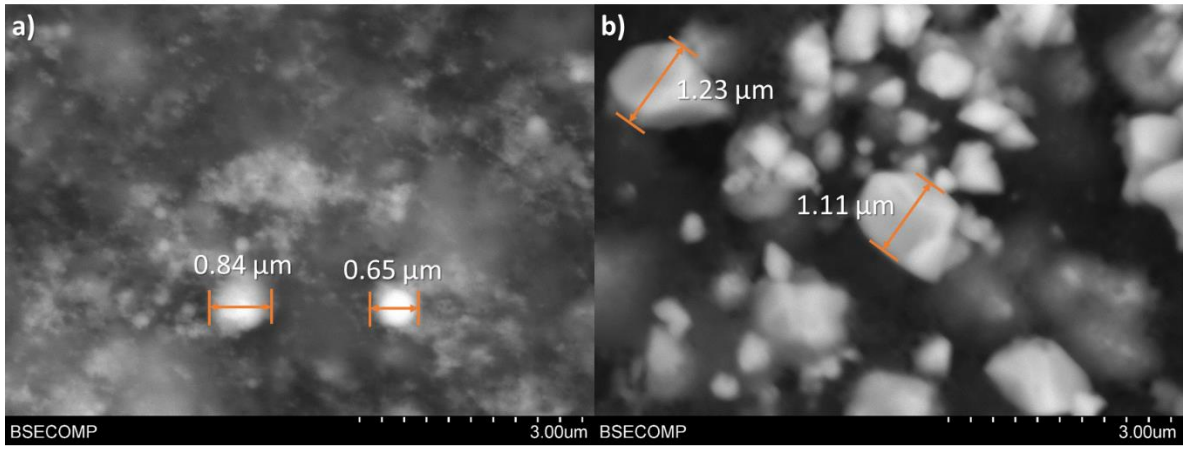

Figure S8. SEM images (16000x magnification back-scattered electrons) of electrode Fe_2O_3-COM/C before (a) and after (b) discharging.

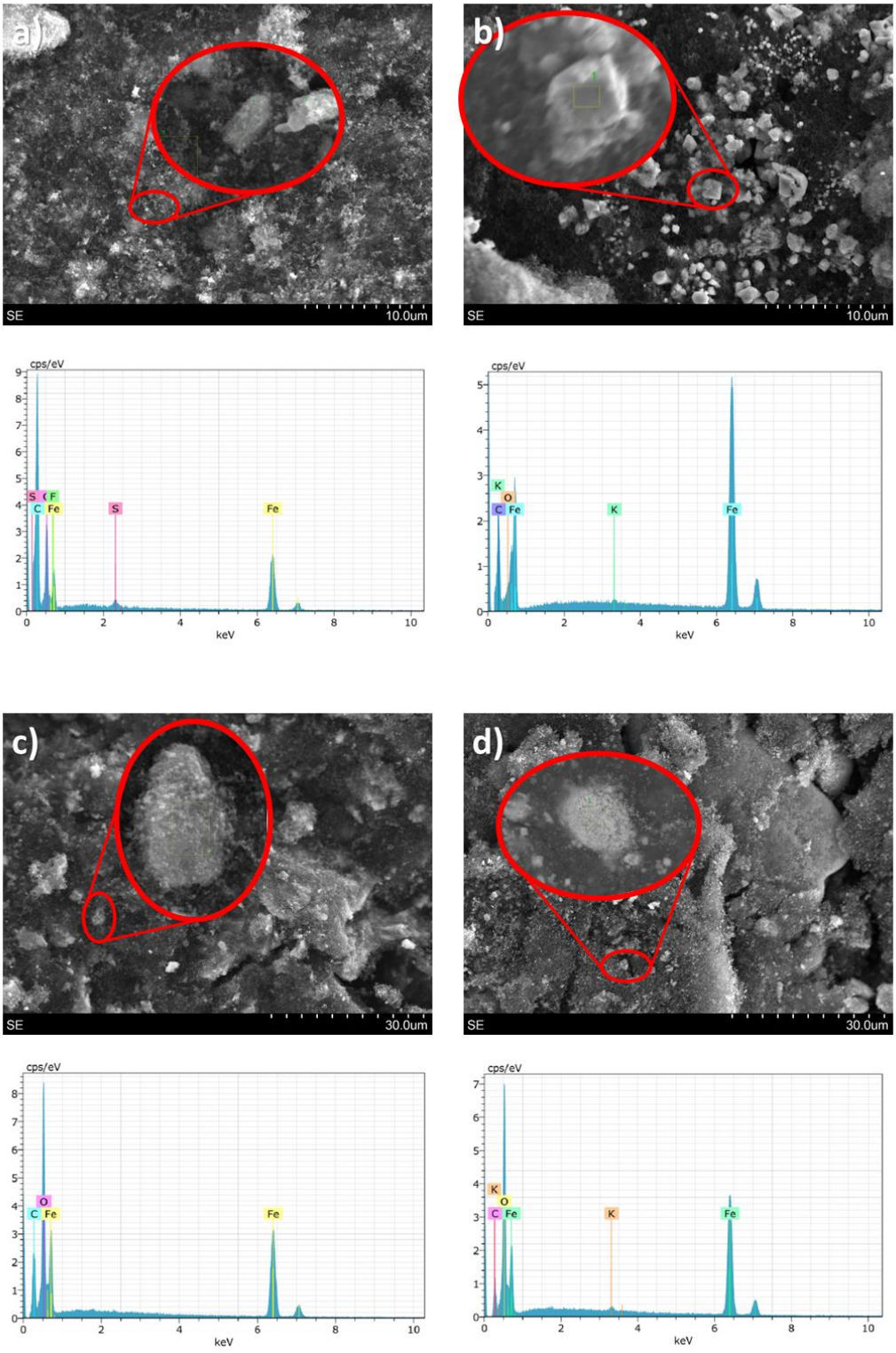

Figure S9. SEM images and EDX analyses for the electrode Fe_2O_3-COM/C: a) fresh electrode and b) after 20 cycles; SEM images and EDX analyses for the electrode S-Fe_2O_3-OXL/C: c) fresh electrode and d) after 20 cycles. Insets are the areas where EDX was measured

S.3. Extended cycling

As stated in the main text, S-Fe_2O_3-SHX/C (**Figure S10**b) increases its capacity during the first 20 cycles, indicating that the material is still not fully activated. According to nitrogen physisorption (Table S2), this oxide has the lowest surface area of all the materials, which means it needs more cycles to increase its area by successive expansions and contractions in order to expose more iron atoms to the electrolyte. After the first 20 cycles, the capacity of the electrode becomes erratic There is a clear tendency to deactivation, but some spikes with high discharge capacity values can be seen (cycles 24, 30, 36, 40, 43). The model estimates a 7 % loss of capacity per cycle, which means a faster deactivation for S-Fe_2O_3-SHX/C than for S-Fe_2O_3-OXL/C (**Figure S10**a). Even though S-Fe_2O_3-SHX has a higher percentage of Sulfur in the bulk (as obtained by elemental analysis), it has less surface Sulfur than S-Fe_2O_3-OXL (Table 1), meaning less sulfate that can reduce to sulfide and help to prevent passivation. Shangguan et al. [7] reached a similar conclusion. Their materials had 5-10 % wt. Sulfur and, and they also reported that the stability and the performance of the electrodes increased with the amount of Sulfur. Another factor for the worse stability of S-Fe_2O_3-SHX when compared to S-Fe_2O_3-OXL is the different crystal size. Being much smaller in the former, this means also a higher tendency to passivation, since small particles are more prone to passivation phenomena than large ones. This manuscript adds another conclusion: it is the amount of Sulfur on the surface, and not necessary in the bulk of the iron oxide the most important property that enhances the stability of the electrode, along with a proper crystal size.

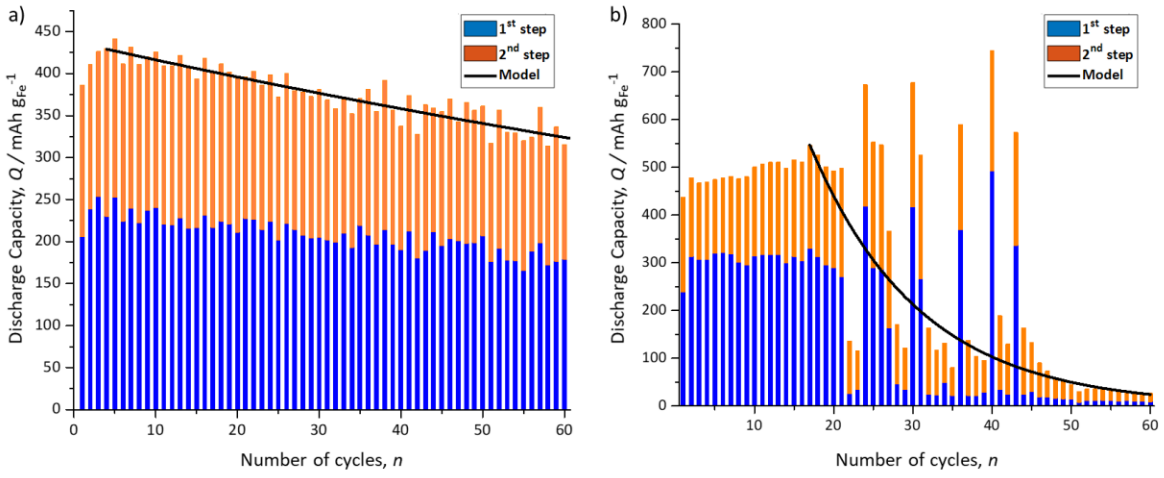

Figure S10. Extended cycling of a) S-Fe_2O_3-OXL; b) S-Fe_2O_3-SHX

To prove the deactivation model adjusted to the first 20 cycles and test the long-term performance of the synthesized materials, a 100-charge-discharge cycles (400 hours) was performed using the most stable material, S-Fe_2O_3-OXL/C. As **Figure S11** shows, the model predicts accurately the behavior of the electrode for *ca.* 70 cycles. From cycle 73 to cycle 74 (green rectangle in **Figure S11**), the capacity decreases circa 14% and never recovers, so the model overestimates the discharge capacity from that moment on. The capacity loss after 100 cycles (350 hours) predicted by the model for this electrode was 39%, while the loss experimentally determined was 49%, still, the model gives an excellent estimation of the behavior of the electrode for 70 cycles. The difference in the expected and experimental values can be attributed to the slight loss of Sulfur along cycling. The amount of Sulfur in the fresh electrode measured by Elemental Analysis was 1.37 wt. %, and upon cycling it slightly decreased to 1.29 wt. %.

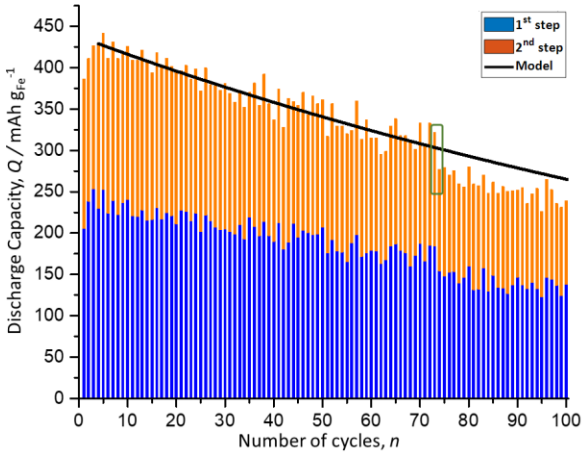

Figure S11. Discharge capacity of the electrode manufactured with Fe_2O_3-OXL-S/C along 100 cycles. Charge rate: 0.4C, discharge rate: 0.2C.

Similar trends can be observed in literature. Tan *et al.*[8] synthesized iron particles embedded in graphitic networks and found out that, after a 30-cycle formation period, the capacity decreases. In that study, the authors attribute the capacity loss to the consumption of sulfide ions, as they use Na_2S 0.01 M as additive in the electrolyte. In fact, they show that the electrodes can recover their capacity by adding again Na_2S to the electrolyte, but other studies have shown that electrolyte additives can poison the positive electrode of iron-air batteries [9]. Other studies show even more look-alike trends. In the paper by Ito *et al.*[10], carbon nanofibers loaded with Fe_3O_4 nanoparticles achieved a maximum of *ca.* 800 mAh g_{Fe}^{-1} at fifth cycle, decreasing their capacity slowly to approx. 650 mAh g_{Fe}^{-1} at 30th cycle, which is roughly a

0.75% capacity loss per cycle. A different but still related deactivation behavior is presented by Manohar *et al.*[11], whose carbonyl iron and bismuth sulfide electrodes showed a remarkable almost 100% charging efficiency for the first 14 cycles, but dropped to 95% in the 15th cycle and did not recover its previous value later on. It must be mentioned that this last study used a discharge rate of 0.05 C, while in the present study it is four times higher.

An electrode manufactured with S-Fe_2O_3-OXL/C was charged at 0.8 C rate and discharged at 0.4 C rate for 34 cycles (**Figure S12**a); and another identical electrode was charged at 1.6 C rate and discharged at 0.8 C rate for 20 cycles (**Figure S12**b). The increase in the charge and discharge C-rates resulted in a high increase in the discharge capacity, especially when charging at 0.8C and discharging at 0.4C (**Figure S12**a). In these conditions, the electrode manufactured with S-Fe_2O_3-OXL/C reached a total of almost 800 mAh g_{Fe}^{-1} of discharge capacity. The highest discharge capacity value we have found in literature is 900 mAh g_{Fe}^{-1} [12], but the performance of the electrodes manufactured in this study is more stable than in the cited article. Especially promising is the maximum of almost 500 mA h g_{Fe}^{-1} in the first discharge plateau. In the case of the electrode cycled at a charge rate of 0.8C and discharge rate of 0.4C (**Figure S12**a), after 17 cycles, a cut-off was applied at 50 minutes of charge for the subsequent cycles. This turned into a slight decrease in discharge capacity, but an important increase in coulombic efficiency (green circle), from 49 % to 62 %, which is a 27 % increase with respect to the efficiency obtained before the charging-time shortening. However, this increase in efficiency comes with a 15 % decrease in the maximum capacity (green circle in **Figure S12**a).

A higher C-rate (**Figure S12**b), namely 1.6 C rate for charging and 0.8 C for discharging, does not increase the capacity of the electrode as much as the intermediate C-rate. Another effect of the increase in the charge and discharge rate is a reduction in the stability factor f for the electrode and a bell-shape curve for maximum discharge capacities (**Figure S12**c). The loss of stability with higher charge and discharge rates was expected and may be due to the formation of goethite with rapid oxidation of iron (II) hydroxide, according to literature [13]. The increase in discharge capacity can seem surprising, but it is a phenomenon that has been previously studied. According to Kitamura et al. [14], this effect in Fe_2O_3/carbon electrodes is explained by the difference of the potentials at which the HER and $Fe(OH)_2$

reduction reach their diffusional limit, being that potential less negative for hydrogen evolution that for iron (II) hydroxide reduction. Additionally, as Weinrich et al. showed with carbonyl iron electrodes [15], a higher charge current can have a positive impact in the formation of the electrodes, as it promotes a higher surface area. However, when the discharge rate is too high, the capacity starts going down. Manohar et al. [11] observed this effect in bismuth-sulfide-doped carbonyl iron electrodes and also found a linear negative correlation between the discharge rate and the discharge capacity.

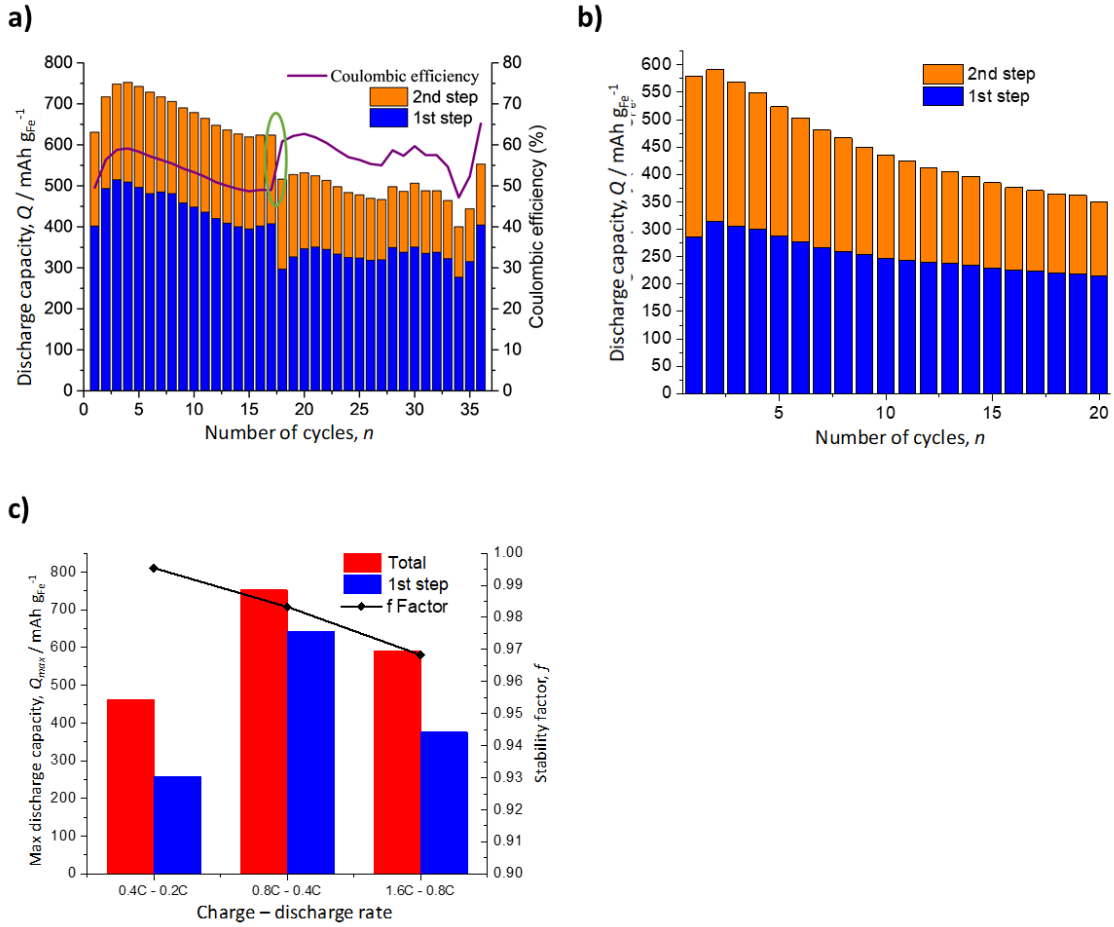

Figure S12. Effect of the charge and discharge C-rate on the electrochemical behavior of electrodes manufactured wit S-Fe_2O_3-OXL/C. a) Charge-discharge cycles of S-Fe_2O_3-OXL at 0.8C rate for charging and 0.4C rate for discharging; b) Charge-discharge cycles of S-Fe_2O_3-OXL at 1.6C rate for charging and 0.8C rate for discharging; c) dependance of maximum capacity and f factor with charge and discharge rates.

The increase in the C-rate also turned into an increase in the charge-discharge potential gap (ΔE) between the charge and discharge plateaus. In **Figure S13**c, ΔE_1 *(black bar)* is the

potential difference between the 1st charge plateau and the 2nd discharge plateau, *i.e.* the potential difference between the oxidation of iron (II) hydroxide to goethite or magnetite and the reduction of these species to iron (II) hydroxide. ΔE_2 (*r*ed bar in **Figure S13**c) is the potential difference between the 2nd charge plateau (reduction of iron (II) hydroxide to metallic iron) and the 1st discharge plateau, which corresponds to the oxidation of metallic iron. From this information, we can deduct that, at low discharge rates (0.2 C - 0.8 C), charge transfer controls the system.

The Butler-Volmer equation (1) indicates that the current increases exponentially with the overpotential, i.e. the overpotential increases logarithmically with the current, and this would explain why increasing the charge-discharge rates from 0.4 C (charge) – 0.2 C (discharge) to 0.8 C (charge) – 0.4 C (discharge) turns into a small increase in the charge-discharge potential gap.

$$i = i_0 \left[\exp\left(-\frac{\alpha z F \eta}{RT}\right) - \exp\left(\frac{(1-\alpha) z F \eta}{RT}\right) \right] \quad (1)$$

On the other hand, when electrochemical reactions are controlled by mass transport or mixed regime, it is necessary a high increase in overpotential to obtain an increase in current, which is what happens when the rates are increased from 0.8 C (charge) – 0.4 C (discharge) to 1.6 C (charge) – 0.8 C (discharge).

In addition, the potential difference between the second charge plateau and the HER was calculated (ΔE_{HER}, **Figure S13**d). The reduction of iron hydroxide and the hydrogen evolution occur simultaneously when the charge and discharge rate are 0.4 C and 0.2 C, respectively. When the C-rate is increased twice fold, the second charge plateau separates some millivolts (around 20) from the HER plateau. By increasing furthermore, the charge rate, this effect magnifies. This could allow us to control HER by varying the charge rate (it would not even be necessary to modify the discharge rate, just the charge rate).

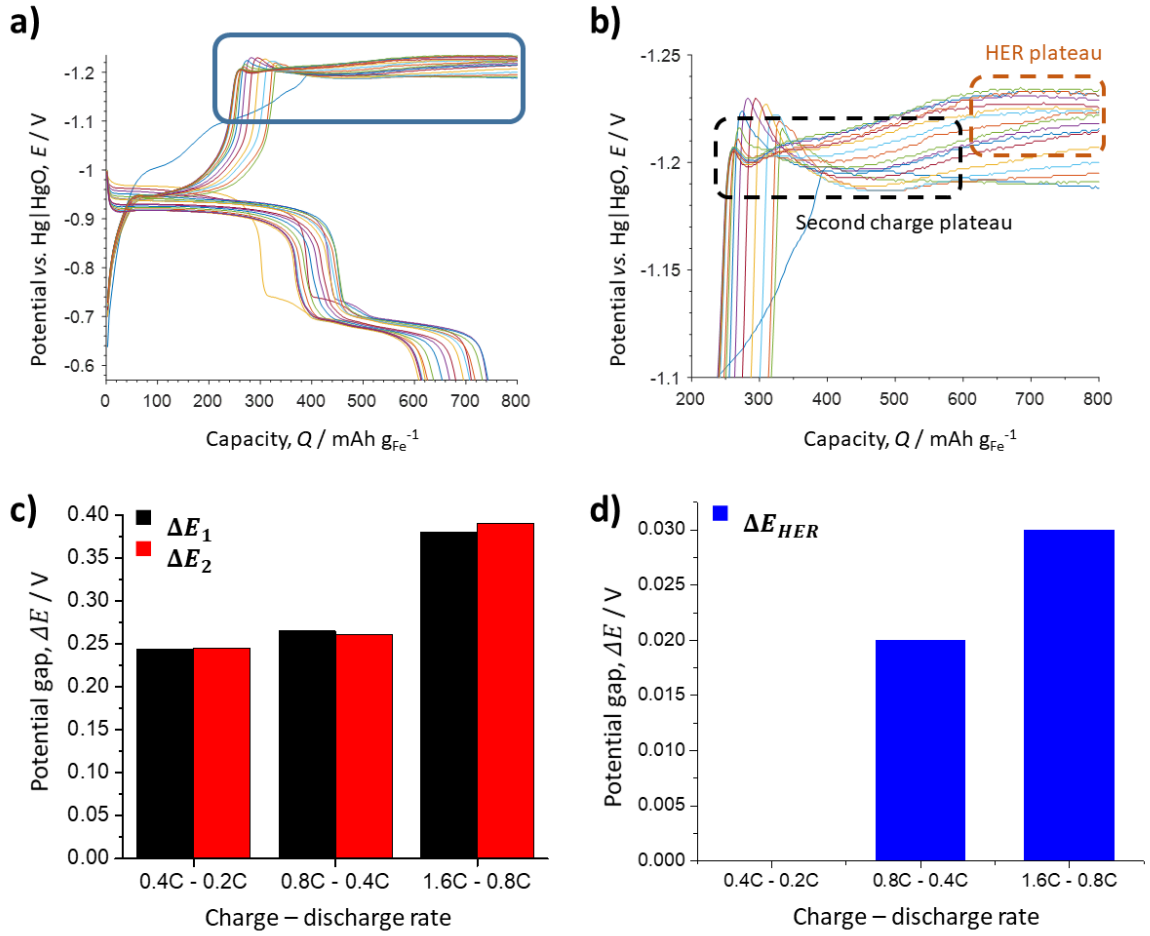

Figure S13. a) 17 first charge and discharge cycles for the S-Fe_2O_3-OXL/C electrode at 0.8C rate for charging and 0.4C rate for discharging. b) Zoom view of the area marked with the rectangle in (a); (c) Average potential gaps for the first and second charge-discharge steps (d) Average potential gap between the second charge plateau and the HER plateau

The increase in coulombic efficiency is a signal that, indeed, most of the HER occurs after the second charge plateau, as seen in the zoomed part of the graph in **Figure S13**b, while almost none of it occurs in the first charge plateau. However, part of the HER takes place together with the charge, and not after it, as can be deducted from the fact that the discharge capacity falls when the charge time is reduced (if the HER took place *after* the charge, reducing the charge time would not affect the charge and, by consequence, the discharge). As expected, the reduction in discharge capacity affects principally the first discharge step (which is related to the second charge step) in the 18th cycle, while the second step retains its capacity. Nonetheless, in the next cycles, the capacity of the first step increases and the one

of the second step slightly decreases, so the ratio of charge between the first and the second discharge steps goes back to 2:1, just like in the beginning of the experiment. The reason for this to happen is that, when the cut-off is applied, the less exposed iron (II) hydroxide molecules cannot be reduced to iron, so less iron atoms can oxidize to iron (II) hydroxide in the next discharge.

(1) Can, M. M.; Ozcan, S.; Ceylan, A.; Firat, T. Effect of Milling Time on the Synthesis of Magnetite Nanoparticles by Wet Milling. *Mater. Sci. Eng. B Solid-State Mater. Adv. Technol.* **2010**, *172* (1), 72–75. https://doi.org/10.1016/j.mseb.2010.04.019.

(2) Chernyshova, I. V.; Hochella, M. F.; Madden, A. S. Size-Dependent Structural Transformations of Hematite Nanoparticles. 1. Phase Transition. *Phys. Chem. Chem. Phys.* **2007**, *9* (14), 1736–1750. https://doi.org/10.1039/b618790k.

(3) Gotić, M.; Musić, S.; Popović, S.; Sekovanić, L. Investigation of Factors Influencing the Precipitation of Iron Oxides from Fe(II) Containing Solutions. *Croat. Chem. Acta* **2008**, *81* (4), 569–578.

(4) Gotić, M.; Musić, S. Mössbauer, FT-IR and FE SEM Investigation of Iron Oxides Precipitated from FeSO4 Solutions. *J. Mol. Struct.* **2007**, *834–836* (SPEC. ISS.), 445–453. https://doi.org/10.1016/j.molstruc.2006.10.059.

(5) Dana, J. D. *System of Mineralogy: V. 1*, 7th ed.; Dana, E. S., Palache, C., Berman, H., Frondel, C., Eds.; Wiley–Blackwell, 1944.

(6) Cazetta, A. L.; Vargas, A. M. M.; Nogami, E. M.; Kunita, M. H.; Guilherme, M. R.; Martins, A. C.; Silva, T. L.; Moraes, J. C. G.; Almeida, V. C. NaOH-Activated Carbon of High Surface Area Produced from Coconut Shell: Kinetics and Equilibrium Studies from the Methylene Blue Adsorption. *Chem. Eng. J.* **2011**, *174* (1), 117–125. https://doi.org/10.1016/j.cej.2011.08.058.

(7) Shangguan, E.; Fu, S.; Wu, C.; Cai, X.; Li, J.; Chang, Z.; Wang, Z.; Li, Q. Sublimed Sulfur Powders as Novel Effective Anode Additives to Enhance the High-Rate Capabilities of Iron

Anodes for Advanced Iron-Based Secondary Batteries. *Electrochim. Acta* **2019**, *301*, 162–173. https://doi.org/10.1016/j.electacta.2019.01.139.

(8) Tan, W. K.; Asami, K.; Maegawa, K.; Kawamura, G.; Muto, H.; Matsuda, A. Formation of Fe-embedded Graphitic Carbon Network Composites as Anode Materials for Rechargeable Fe-air Batteries. *Energy Storage* **2020**, *2* (6). https://doi.org/10.1002/est2.196.

(9) McKerracher, R. D.; Figueredo-Rodriguez, H. A.; Dimogiannis, K.; Alegre, C.; Villanueva-Martinez, N. I.; Lázaro, M. J.; Baglio, V.; Aricò, A. S.; Ponce de León, C. Effect of 1-Octanethiol as an Electrolyte Additive on the Performance of the Iron-Air Battery Electrodes. *J. Solid State Electrochem.* **2021**, *25* (1), 225–230. https://doi.org/10.1007/s10008-020-04738-4.

(10) Ito, A.; Zhao, L.; Okada, S.; Yamaki, J. I. Synthesis of Nano-Fe3O4-Loaded Tubular Carbon Nanofibers and Their Application as Negative Electrodes for Fe/Air Batteries. *J. Power Sources* **2011**, *196* (19), 8154–8159. https://doi.org/10.1016/j.jpowsour.2011.05.043.

(11) Manohar, A. K.; Malkhandi, S.; Yang, B.; Yang, C.; Surya Prakash, G. K.; Narayanan, S. R. A High-Performance Rechargeable Iron Electrode for Large-Scale Battery-Based Energy Storage. *J. Electrochem. Soc.* **2012**, *159* (8), A1209–A1214. https://doi.org/10.1149/2.034208jes.

(12) McKerracher, R. D.; Figueredo-Rodriguez, H. A.; Alegre, C.; Aricò, A. S.; Baglio, V.; Ponce de León, C. Improving the Stability and Discharge Capacity of Nanostructured Fe2O3/C Anodes for Iron-Air Batteries and Investigation of 1-Octhanethiol as an Electrolyte Additive. *Electrochim. Acta* **2019**, *318*, 625–634. https://doi.org/10.1016/j.electacta.2019.06.043.

(13) Balasubramanian, T. S.; Vijayamohanan, K.; Shukla, A. K. Mechanisms of the Discharge of Porous-Iron Electrodes in Alkaline Medium. *J. Appl. Electrochem.* **1993**, *23* (9), 947–950. https://doi.org/10.1007/BF00251032.

(14) Kitamura, H.; Zhao, L.; Hang, B. T.; Okada, S.; Yamaki, J. Effect of Charge Current

Density on Electrochemical Performance of Fe/C Electrodes in Alkaline Solutions. *J. Electrochem. Soc*. **2012**, *159* (6), A720–A724. https://doi.org/10.1149/2.049206jes.

(15) Weinrich, H.; Gehring, M.; Tempel, H.; Kungl, H.; Eichel, R. A. Impact of the Charging Conditions on the Discharge Performance of Rechargeable Iron-Anodes for Alkaline Iron–Air Batteries. *J. Appl. Electrochem.* **2018**, *48* (4), 451–462. https://doi.org/10.1007/s10800-018-1176-4.